



N-well resistance modelling in Q -factor of doughnut-shaped PN varactors

M. Marrero-Martín, B. González, J. García and A. Hernández

Institute for Applied Microelectronics, Universidad de Las Palmas de Gran Canaria
 Edificio de Electrónica y Telecomunicación (Pabellón A)
 Campus Universitario de Tafira. 35017 – Las Palmas, Spain
 e-mail: benito@iuma.ulpgc.es
 Phone: 34-928452875 Fax: 34-928451243

Abstract: In this paper the N-well resistance in doughnut-shaped PN varactors, with the cathode connected to an N^+ buried layer, has been modelled. The proposed expression for the N-well resistance, numerically validated, is based on the device geometry and overlapping of adjacent basic cells, and adequately reproduces its applied reverse bias voltage dependency. Once the varactor extrinsic parasitic components are extracted considering proximity effects, from anode-to-cathode measured RF admittances, and frequencies ranging from 0.5 GHz to 10 GHz, the impact of the N-well resistance on the experimental varactor quality factor is determined for reverse biases up to 5 V.

Keywords: PN varactor, N-well resistance, physically-based modelling, Q -factor.

1. Introduction

Varactors are part of many RF integrated circuits, such as voltage controlled oscillators [1–4], whose resonance frequency diminishes with the varactor capacitance, C , as $1/\sqrt{LC}$, where L stands for the LC tank inductance. Precise physical models for PN junction capacitances have been reported [5–13], but not for the junction parasitic resistances and, consequently, neither for the PN varactor quality factor.

The varactor quality factor, Q , is given by $1/(2\pi fRC)$, R being the equivalent series resistance and f the operating frequency. In PN junctions the series resistance can be high enough to drastically reduce the varactor quality factor for millimetre-wave applications, degrading the LC tank global quality factor [14].

The equivalent PN series resistance rises due to the increase of the N-well resistance, which is studied here. Thus, with permanently modulated depletion capacitance, the smaller the distance between N^+ and P^+ terminal diffusions is, the better the quality factor of the varactor that results.

In order to achieve $0.45 \text{ fF}/\mu\text{m}^2$ for the capacitance–area aspect ratio (at null applied bias voltage), PN junction varactors are built up by overlapping adjacent doughnut-shaped basic cells (BCs) [5]. In the middle of every BC a deep central N^+ diffusion (similar to that for BJT collectors) connects the cathode terminal to an N^+ buried layer. Around the central N^+ diffusion (see figure 1(a)), a rectangular P^+ diffusion is located to form the anode. Overlapping takes place along both side lengths of adjacent P^+ diffusions, as figure 1(b) shows for a varactor with 7×6 BCs.

In this paper we evaluate the N-well resistance, R_{nw} , in doughnut-shaped PN varactors. The varactors fabricated for that purpose, and their measurement methodology, are explained in Section 2. In Section 3 we propose a model for R_{nw} , the expression of which is validated through numerical simulations in Section 4. Extrinsic parasitic components are extracted in Section 5, where the impact of R_{nw} on the experimental quality factor of varactors is also analysed. Finally, conclusions are given in Section 6.



2. Fabrication and measurements

Three varactors have been designed using the 0.35 μm SiGe standard process for RF applications [15]: V1, V2, and V3 with 7×6 BCs, 12×5 BCs, and 10×9 BCs, respectively, which layouts are represented in figure (2). All of them include the measurement structures required by the Cascade GSG microprobes (*i.e.* devices under test – DUT – are surrounded by a guard-ring containing measuring pads; see photo of V2 in figure (2)), and have been measured with the Agilent 8720ES Vector Network Analyzer. To calibrate the measurement system, the short-open-load-through method is implemented in a previous step. Three additional structures, single-open, single-short and thru, have been designed to perform the subsequent de-embedding technique [16], based on that with four steps in [17], eliminating the parasitic effects introduced by pads and the guard-ring. Finally, a reverse bias voltage (from cathode to anode), V_r , up to 5 V has been applied, in the 0.5 GHz to 10 GHz frequency range.

3. Model for R_{nw}

The anode-to-cathode electrical performance of PN varactors can be modelled with the (successfully applied to MOS varactors in [14]) simple equivalent circuit of figure 3, where R_c and L account for the ohmic contact losses and the series inductance caused by the metal lines from anode (A) to cathode (C), respectively; C_p is the parasitic capacitance between metal ports, and C_j represents the junction capacitance associated with the N-well depletion region (for P⁺N junctions); expressions for C_p and C_j to be used in this work, depending on the number of BCs, were already obtained in [5]. Finally, R_{nw} is the N-well resistance to be modelled.

The varactor series resistance from anode-to-cathode, when extracted, is usually attributed to ohmic contact losses only [6, 7, 9–12], neglecting the influence of N-well resistance. However, this is what we want to determine through the varactor quality factor evaluation.

We are considering the following contributions to the N-well resistance in doughnut-shaped PN varactors with a buried layer:

- resistances from the internal lateral edges of the P⁺ diffusion in BCs, to the closer side of the central N⁺ diffusion: R_{nw-1} and R_{nw-2} (see figure 4), and
- the resistance from the bottom of the P⁺ diffusions to the N⁺ buried layer, through a P⁺ equivalent centralized area: R_{nw-3} (see figure 5 for 2×2 BCs).

With these main contributions, the N-well varactor resistance is approximated by

$$\frac{1}{R_{nw}} = \frac{N}{R_{nw-1}} + \frac{N}{R_{nw-2}} + \frac{1}{R_{nw-3}}, \quad (1)$$

as all resistances involved are connected in parallel, with N being the number of BCs. Expressions for these components are obtained as reported in the following subsections.

3.1 N-well resistances to the central N⁺ diffusion

For a BC the transversal area of the R_{nw-1} and R_{nw-2} resistive paths, S_1 and S_2 , respectively, can be written as



$$S_i = 2 \cdot \left(e + c - \frac{e}{s-w} \cdot y_i \right) \cdot (d_i + 2y_i), \quad i = 1, 2, \quad (2)$$

where the meaning of the geometrical parameters is expressed in figures 1(a), 4(a), and 4(b): s is the distance between the internal P⁺ lateral edges and the central N⁺ diffusion, e stands for the separation between the bottom of the P⁺ diffusion and the N⁺ buried layer, c is the P⁺ diffusion depth, and d_1 and d_2 indicate the cross-section lengths of the central N⁺ diffusion (the actual values for all these parameters are given in table 1); y_i ($i = 1, 2$) represents the transversal area location from the corresponding edge of the central N⁺ diffusion, and w is the depletion width correction (see figure 4(b)), which is given by

$$w = \frac{\epsilon_{Si}}{C_A} \sqrt{1 + \frac{V_r}{V_{bi}}}, \quad (3)$$

with ϵ_{Si} standing for the silicon permittivity, C_A (1.42 fF μm^{-2}) is the PN junction capacitance per unit area, and V_{bi} (1.01 V) the built-in voltage [5].

By integrating between the P⁺ and the central N⁺ diffusions, R_{nw-i} ($i = 1, 2$) results:

$$R_{nw-i} = \int_0^{s-w} \frac{\rho}{S_i} \cdot dy_i = \frac{\rho(s-w)}{4(s-w)(c+e) + 2d_i e} \cdot \ln \frac{(d_i + 2s - 2w)(c+e)}{cd_i}, \quad i = 1, 2, \quad (4)$$

ρ (0.049 $\Omega\cdot\text{cm}$) being the silicon N-well resistivity, considering the degradation of the transport properties by phonon scattering and Coulomb scattering due to ionized impurities [7].

3.2 N-well resistance to the N⁺ buried layer

In order to evaluate R_{nw-3} , we substitute the bottom of the P⁺ diffusions by an equivalent centralized rectangular surface of the same area, $a_1 \times a_2$, with identical aspect ratio to that of the buried layer horizontal dimensions, $b_1 \times b_2$ (*i.e.* $a_1/a_2 = b_1/b_2$), excluding the depletion width from the distance to the buried layer, $e-w$. See figure 5, where a_1 , a_2 , b_1 , and b_2 are represented. Their values, for all varactors, are summarized in table 2.

Thus, the transversal area of the R_{nw-3} resistive path, S_3 , can be written as

$$S_3 = \left(b_1 - \frac{b_1 - a_1}{e-w} z \right) \cdot \left(b_2 - \frac{b_2 - a_2}{e-w} z \right), \quad (5)$$

with z being the transversal area location from the buried layer (see figure 5). All in all, R_{nw-3} results in the following expression:

$$R_{nw-3} = \int_0^{e-w} \frac{\rho}{S_3} \cdot dz = \frac{\rho(e-w)}{a_2(b_1 - a_1) - a_1(b_2 - a_2)} \cdot \ln \frac{a_2 b_1}{a_1 b_2}, \quad (6)$$



4. Numerical validation

Making use of Sentaurus Device [18], the N-well resistance has been numerically simulated excluding the depletion region, w width, from the N-well. Based on arguments of electrical symmetry [19], the resulting structure can be reduced by a quarter (as figure 1(b) indicates), where Poisson and current continuity equations are solved auto-consistently. Thus, after the customary optimization procedures to correctly describe the electrostatic potential within R_{nw} , around 3×10^5 mesh points per structure are obtained.

Varying w and taking into account (3), the resulting R_{nw} voltage dependence is shown in figure 6 for V1 (as solid line with squares), V2 (as dashed line with circles), and V3 (as dotted line with triangles). The corresponding modelled data are similarly represented, excluding symbols. In all cases the N-well resistance slightly diminishes with the reverse bias, because small variations of the depletion region width are expected (lower than $0.1 \mu\text{m}$, for the N-well doping concentration). Notice that our model underestimates R_{nw} , which is more evident at low reverse biases, and when the number of BCs diminishes. However, the relative error between the numerical and modelled data always remains lower than 9.3%, in all varactors. Therefore, expression (1), with (4) and (6), can be used as a satisfactory approximation for the N-well resistance.

5. Impact of R_{nw} on the quality factor of the varactor

Once R_{nw} has been numerically validated, we proceed to determine the impact of R_{nw} on the quality factor of the varactor, defined by:

$$Q = \frac{\left| \text{Im} \left(\frac{1}{Y_{AC}} \right) \right|}{\text{Re} \left(\frac{1}{Y_{AC}} \right)}, \quad (7)$$

where Y_{AC} stands for the anode-to-cathode admittance. From the equivalent circuit of figure 3 it can be written

$$\left| \text{Im} \left(\frac{1}{Y_{AC}} \right) \right| = \frac{\omega^2 R_{nw}^2 C_p^2 C_j^2 + C_p (C_j + C_p)}{\omega C_p \left[\omega^2 R_{nw}^2 C_p^2 C_j^2 + (C_j + C_p)^2 \right]} - \omega L \quad (8)$$

and

$$\text{Re} \left(\frac{1}{Y_{AC}} \right) = R_c + \frac{R_{nw} C_j^2}{\omega^2 R_{nw}^2 C_p^2 C_j^2 + (C_j + C_p)^2}. \quad (9)$$

For any varactor $(C_j + C_p)^2 > C_p (C_j + C_p) \gg \omega^2 R_{nw}^2 C_p^2 C_j^2$ in the frequency and voltage ranges under study. Thus, (8) and (9) can be reduced, respectively, to



$$\left| \text{Im} \left(\frac{1}{Y_{AC}} \right) \right| \approx \frac{1}{\omega(C_j + C_p)} - \omega L \quad (10)$$

and

$$\text{Re} \left(\frac{1}{Y_{AC}} \right) \approx R_c + R_{nw} \left(\frac{C_j}{C_j + C_p} \right)^2. \quad (11)$$

Therefore, by substituting (10) and (11) in (7), the quality factor can be rewritten as:

$$Q \approx \frac{C_j + C_p}{R_c (C_j + C_p)^2 + R_{nw} C_j^2} \cdot \frac{1}{\omega} - \frac{\omega L (C_j + C_p)^2}{R_c (C_j + C_p)^2 + R_{nw} C_j^2}. \quad (12)$$

Figure 7(a) shows the measured anode-to-cathode RF resistance, $\text{Re}(1/Y_{AC})$, for V1 (with circles), V2 (with triangles) and V3 (with squares), from 0.5 GHz to 10 GHz with 1 V reverse bias. Note that the data fluctuate considerably below 4 GHz, which was attributed in [20] to the small and close values of the junction and contact resistances, R_{nw} and R_c , and the relative low frequencies. Above 4 GHz a frequency squared dependency can clearly be observed with V2 and V3, which is attributed to a proximity-related metallization resistance (no relevant magnetic coupling seems to appear for the smaller varactor, V1, with shorter metal lines) [21–23]. Skin effects, with related resistance proportional to the square root of frequency, are not appreciated. Therefore, R_c can be approximated by:

$$R_c \approx R_{dc} (1 + \alpha f^2) \quad (13)$$

where f is the operating frequency, and R_{dc} and α being the low frequency extrinsic resistance and a fitting coefficient, respectively, which are determined fitting $\text{Re}(1/Y_{11})$ measured above 4 GHz, making use of (11) and the numerical N-well resistances. On average, the resulting values in the voltage range under consideration are shown in table 3 for every varactor. Notice that, as expected, the higher the number of BCs is, the lower R_c turns out to be [11, 14]. However, because of its longer metal lines (compare layouts of varactors V1 and V2 in figure 2) a weak reduction is observed for V2. Thus, the modelled anode-to-cathode RF resistance above 4 GHz at 1 V reverse bias, making use of (11) and (13), is represented in Figure 7(a) with solid, dashed, and dotted lines for V1, V2, and V3, respectively. In all cases the relative error between $\text{Re}(1/Y_{AC})$ measured and modelled is lower than 3.7% on average (up to 10 GHz).

Regarding series inductance caused by the metal line on the P^+/N^+ diffusions, L , it is determined based on the slope of the plot of $\omega \times |\text{Im}(1/Y_{AC})|$ versus ω^2 , as figure 7(b) indicates for 1 V reverse bias. Measured data are represented with crosses, and linear fitting adjustments with solid line, dashed line, and dotted line for V1, V2, and V3, respectively. The obtained inductances are summarized in table 3, with a superior value for V2, with the longest metal lines.

Then, once the extrinsic parasitic elements are known, the quality factor (12) is evaluated with the modelled R_{nw} (1), making use of (4) and (6). The resulting modelled (as solid line, dashed line, and dotted line for V1, V2, and V3, respectively) and



measured (as squares, circles, and triangles for V1, V2, and V3, respectively) quality factors are shown in figure 8(a), for a representative operating frequency of 5 GHz. In a similar way, the corresponding modelled data excluding R_{nw} (with $R_{nw} = 0$ in (12)) are also represented by crosses. In all varactors, the dependence of Q on the applied bias voltage is correctly predicted by our model: the higher reverse voltage gives superior quality factor, with a relative error lower than 3.5%, which is not the case neglecting R_{nw} , when the quality factor is overestimated. Additionally, even when the parasitic components are smaller for V3, its quality factor is similar to that for V2, as the capacitance for V3 is superior.

Finally, as figure 8(b) shows, similar results are obtained for an operating frequency of 10 GHz, when proximity effects enhance. Nevertheless, in this case the impact of excluding R_{nw} is less relevant (lower Q -factors are involved), but shows relative errors still as higher as 17%.

6. Conclusions

A physical-based model to calculate the N-well resistance in PN doughnut-shaped varactors with N^+ buried layer is proposed. Our model has been numerically validated, and incorporates internal geometrical parameters and a number of BCs. The reported model adequately predicts the bias voltage dependence through the N-well depletion region modulation. Furthermore, an expression to accurately predict the varactor quality factor has been derived, considering proximity effects, for which the incorporation of R_{nw} is essential. Finally, the modelling approach reported can be easily incorporated as an add-on in circuit simulators, proportionating detailed quality factor selection criteria to RF circuit designers.

Acknowledgments

This work was developed thanks to the Research Projects TEC2011-28357-C02-02 and TEC2011-28724-C03-02.

References

- [1] N. Pohl, H.-M. Rein, T. Musch, K. Aufinger, J. Hausner, *IEEE J Solid-St Circ*, 44 (2009) 2655–62.
- [2] M. Marrero-Martín, B. Gonzalez, J. Garcia, S.L. Khemchandani, A. Hernandez, J. del Pino, *Int J Electron*, 99 (2012) 1165–78.
- [3] J.-J. Kuo, Z.-M. Tsai, P.-C. Huang, C.-C. Chiong, K.-Y. Lin, H. Wang, *IEEE Microwave and Wireless Components Lett*, 19 (2009) 653–5.
- [4] F. Padovan, M. Tiebout, K. Mertens, A. Bevilacqua, A. Neviani, A SiGe bipolar VCO for backhaul E-band communication systems. In: *Proc of ESSCIRC 2012*: 402–5.
- [5] M. Marrero-Martín, J. García, B. González, A. Hernández, *Int J Numer Model*, 23 (2010) 364–78.
- [6] Y. Ahn, K. Han, H. Shin, *Jpn J Appl Phys*, 42 (2003) 2110–3.
- [7] S.M. Sze, *Physics of Semiconductor Devices*, second ed., Wiley, New York, 1981.
- [8] V.M. Ioffe, S.I. Chikichev, *Solid-State Electron*, 49 (2005) 385–97.



- [9] S.C. Kelly, J.A. Power, M. O'Neill, *IEEE Trans Semiconductor Manufacturing*, 17 (2004) 142–9.
- [10] A.-S. Porret, T. Melly, C.C. Enz, E.A. Vittoz, Fellow, *IEEE J Solid-St Circ*, 35 (2009) 337–45.
- [11] M.-H. Tsai, S.-K. Huang, S.H.S. Hsu, *Jpn J Appl Phys*, 52 (2013) 04CE09.
- [12] V.I. Cojocaru, T.J. Brazil, A large-signal equivalent circuit model for hyperabrupt P-N junction varactor diodes. In: *Proc of Microwave Conference 1992*: 1115–21.
- [13] A.N. Tulenev, Generalized mathematical model of the varactor diode, In: *Proc of EDM 2003*: 91–4.
- [14] Y. Oh, J.-S. Rieh, *IEEE Trans Microw Theory and Techniques*, 59 (2011) 1520–9.
- [15] Austria Micro System (AMS), 0.35 μm HBT BiCMOS process parameters, 2005.
- [16] I. Gutiérrez, J. Meléndez, J. García, I. Adin, G. Bistue, J. de No, *Lat Am Trans IEEE*, 3 (2005) 15–20.
- [17] T.E. Kolding, *IEEE Trans Electron Devices*, 47 (2000) 734–40.
- [18] Sentaurus Device User Guide, Version D-2010.03.
- [19] S. Kolluri, K. Endo, E. Suzuki, K. Banerjee, Modeling and analysis of self-heating in FinFET devices for improved circuit and EOS/ESD performance. In: *Proc of IEDM 2007*: 177–80.
- [20] Y.-T. Lai, The study of junction varactor and CMOS varactor for radiofrequency voltage control oscillator applications, PhD Dissertation, National Cheng Kung University, Taiwan, 2004.
- [21] W.B. Kuhn, N.M. Ibrahim, *IEEE Trans Microwave Theory and Techniques*, 49 (2001) 31–8.
- [22] G.K. Felic, D. Ng, E. Skafidas, *IEEE Trans Magnetics*, 49 (2013) 1353–60.
- [23] W. Schoenmaker, P. Meuris, E. Janssens, M. Verschaeve, *Solid-State Electron*, 49 (2005) 747–54.



FIGURES

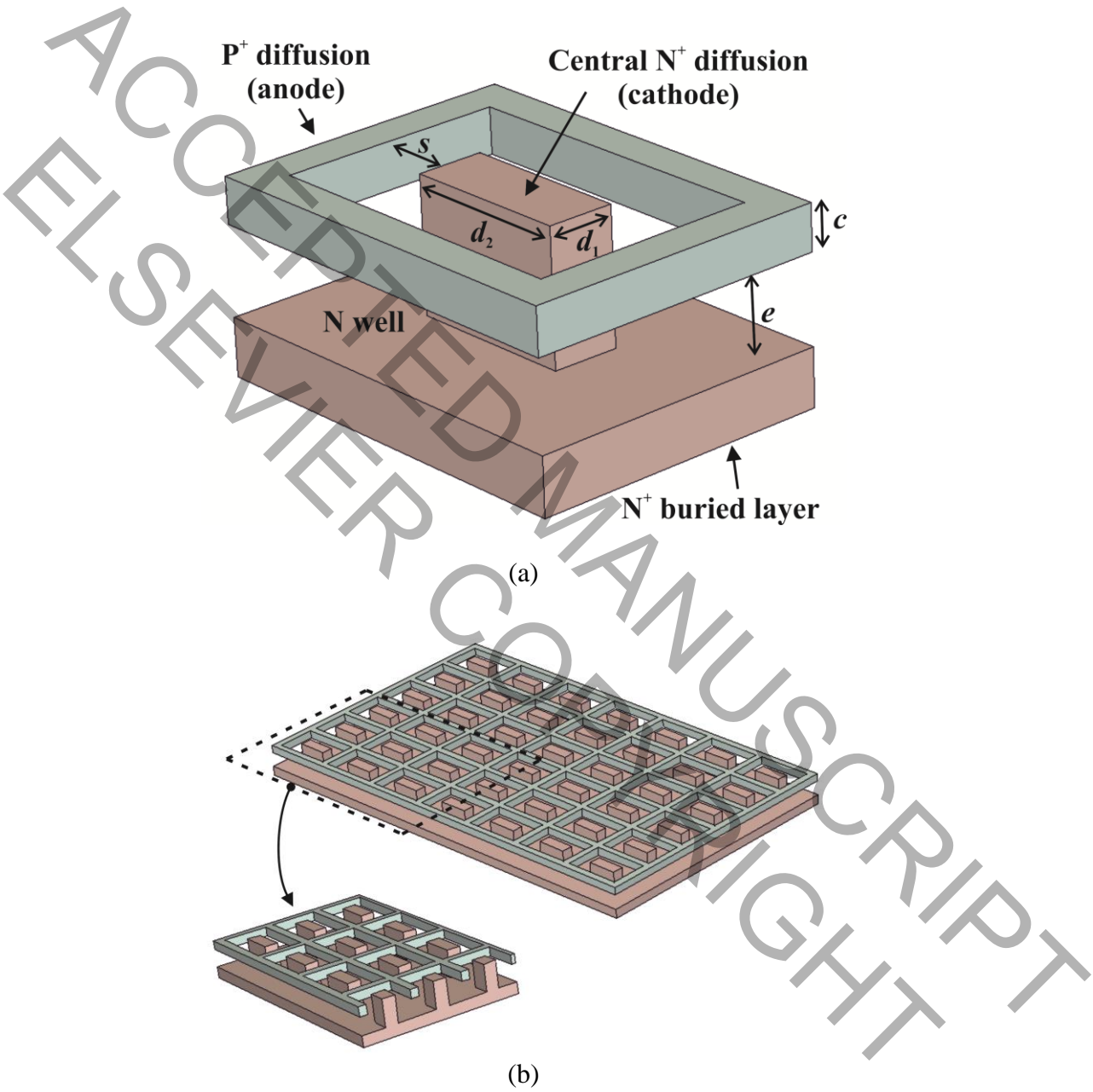


Figure 1

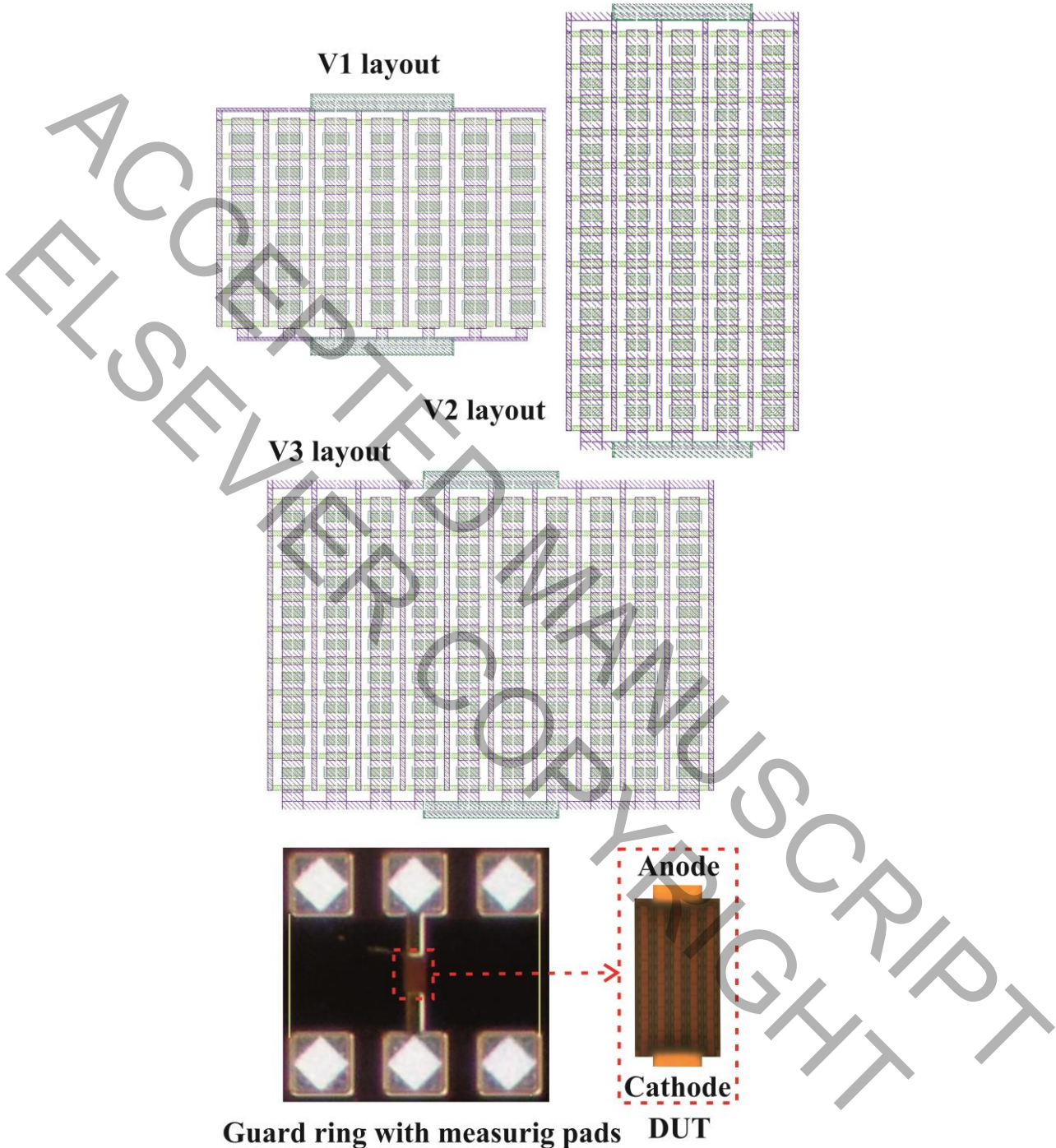


Figure 2

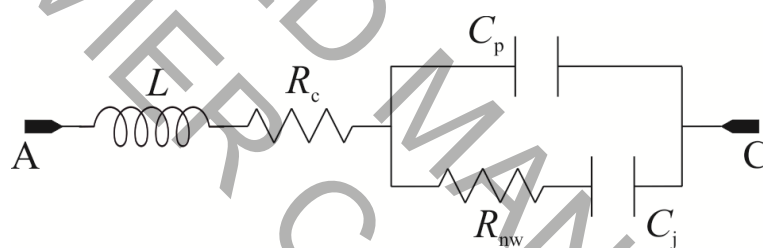


Figure 3

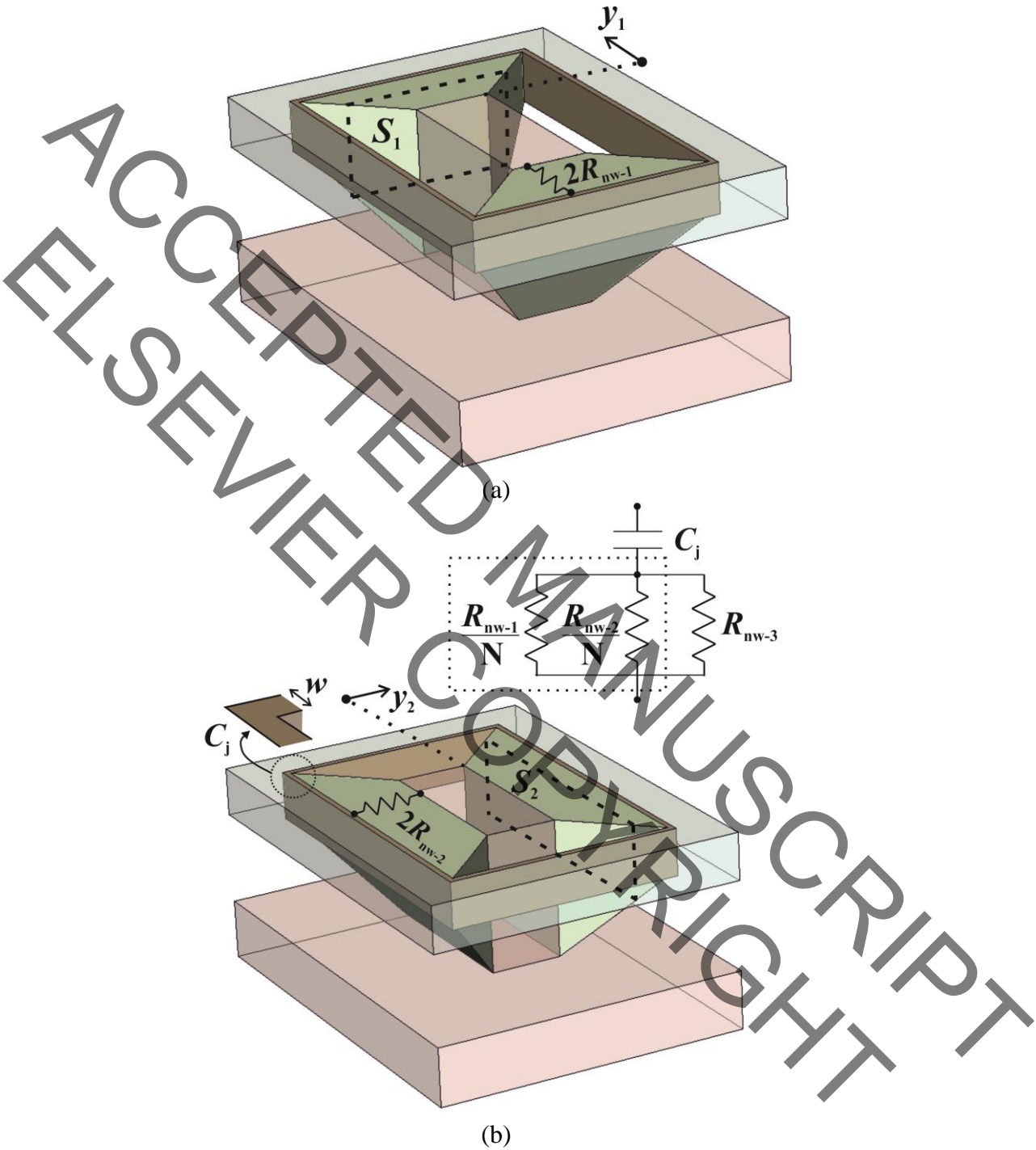
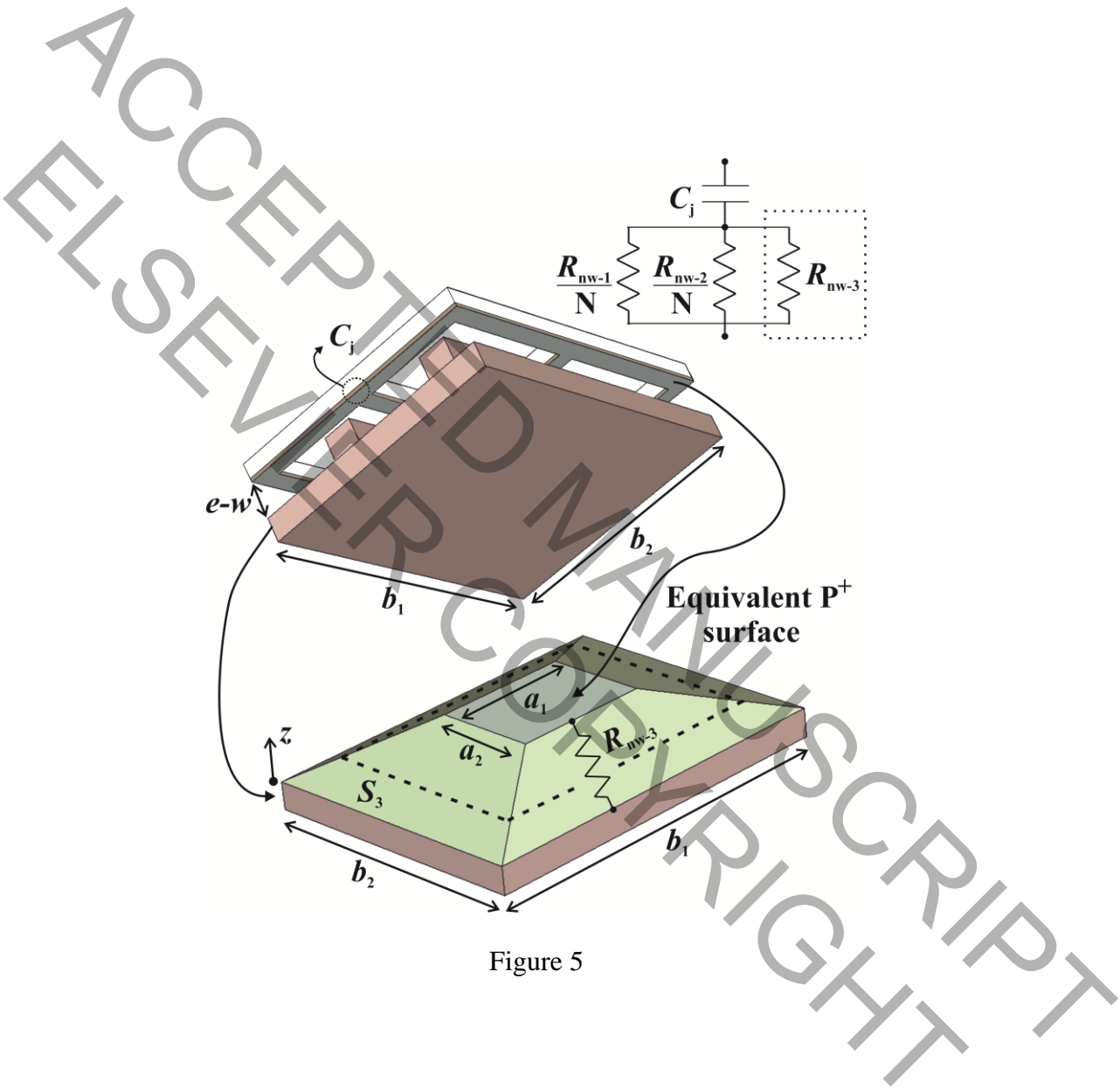
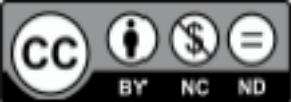


Figure 4





ACCEPTED MANUSCRIPT
EELSEVIER
COPYRIGHT

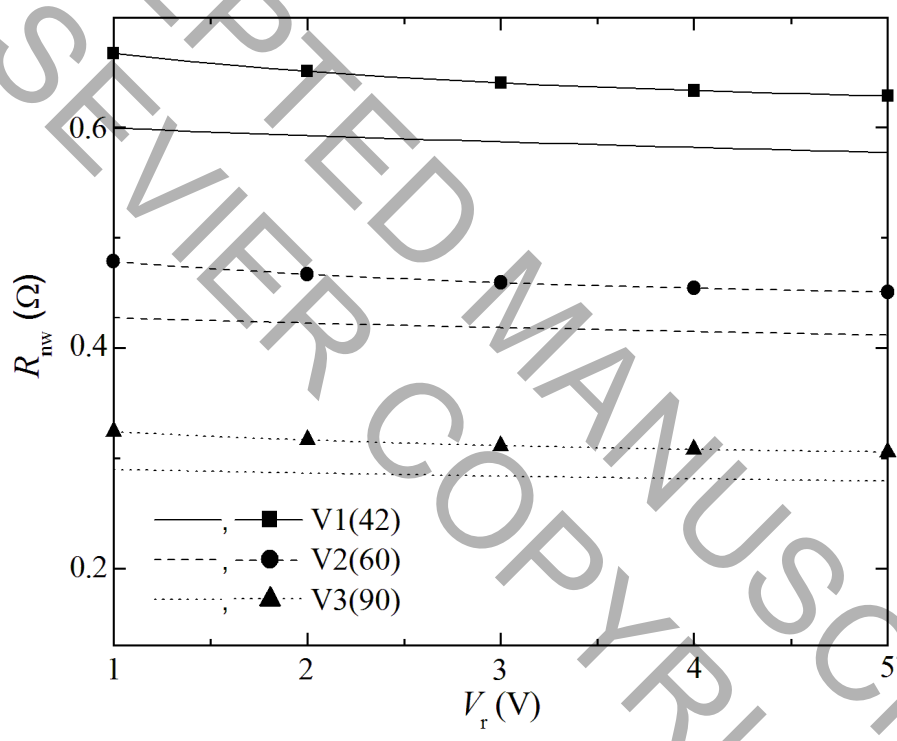


Figure 6

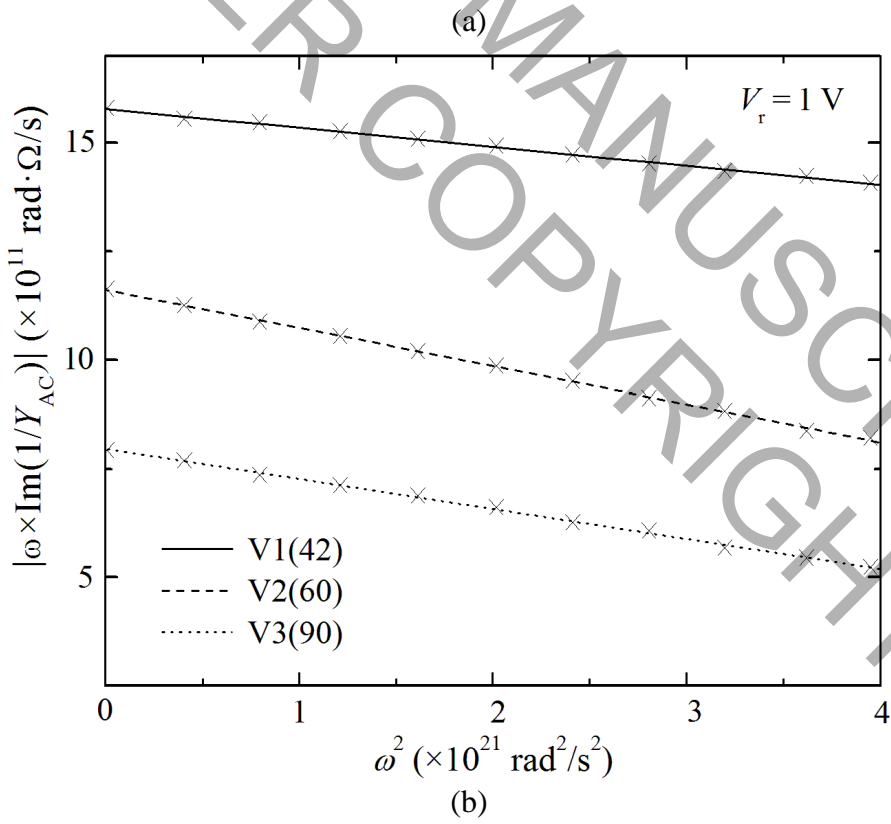
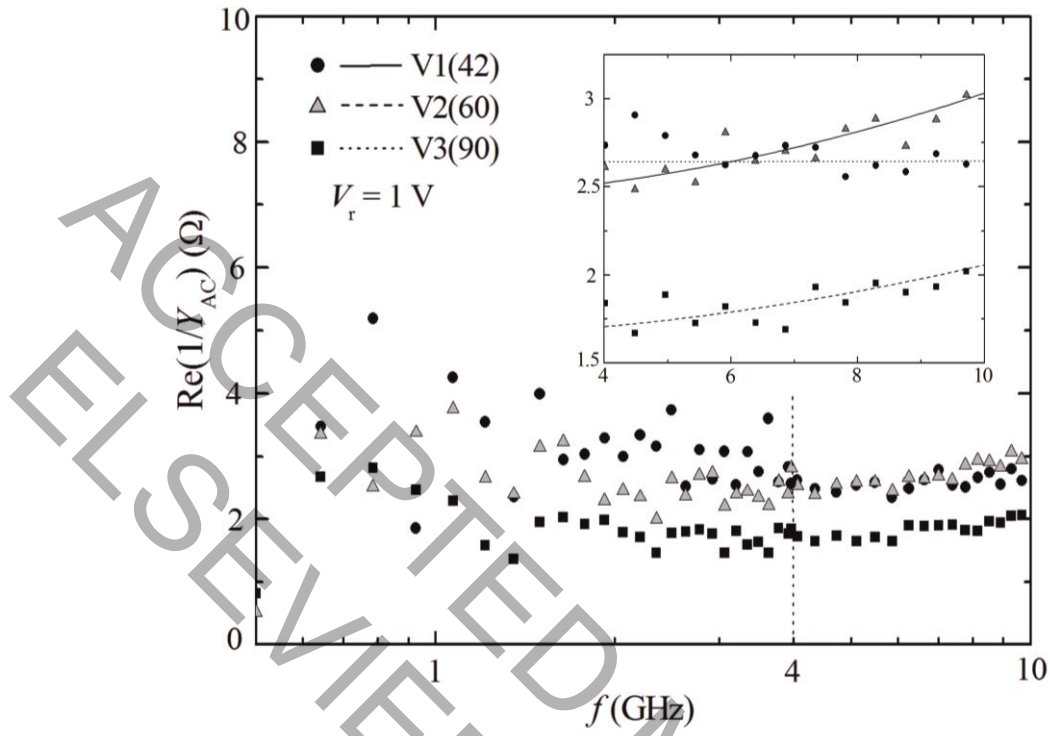


Figure 7

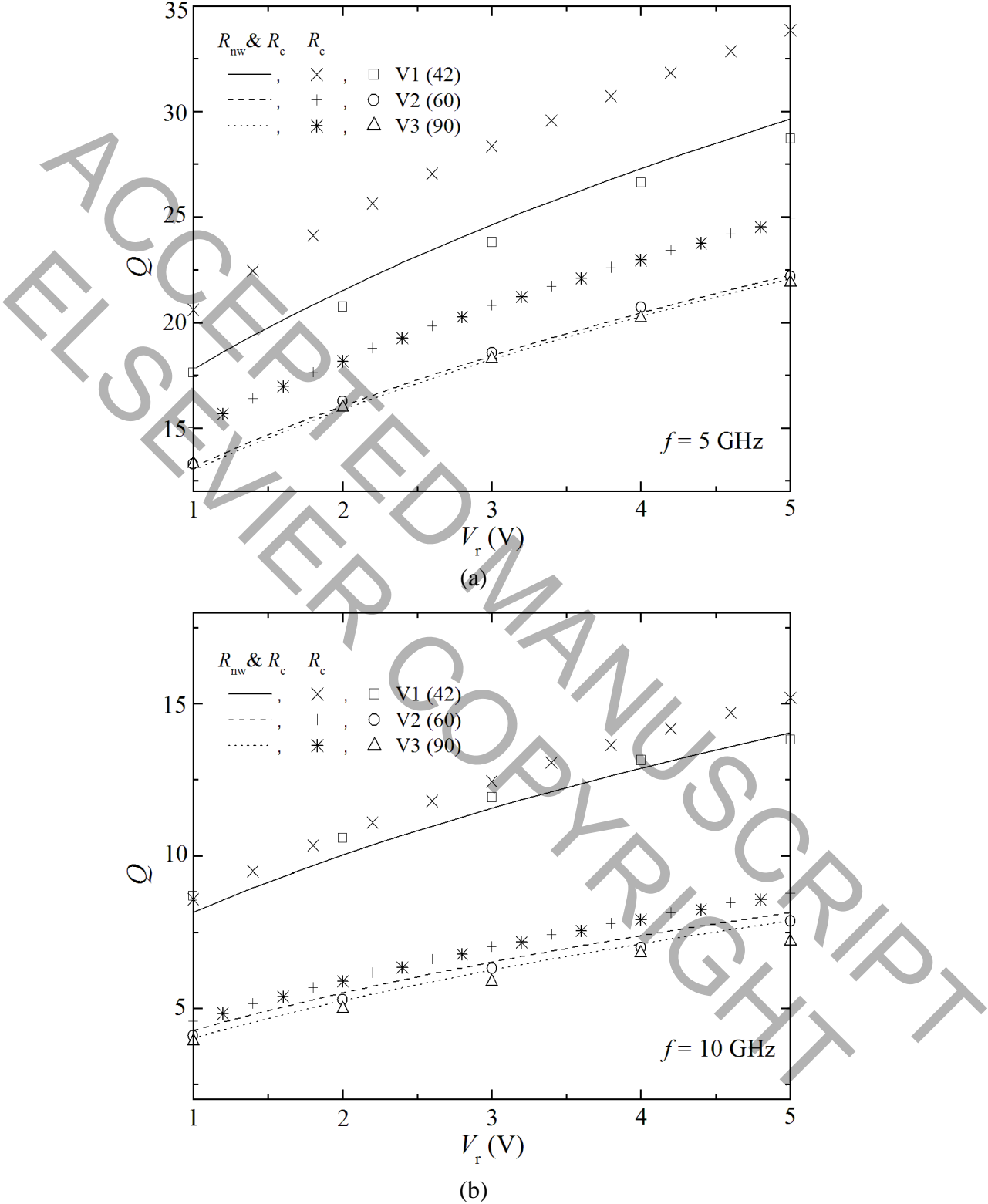
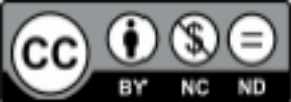


Figure 8



LEGENDS

Figure 1: (a) Basic cell (BC) of the varactors. (b) A varactor with 7×6 BCs and detached quarter (with dashed lines) for simulation purposes.

Figure 2: Layouts of varactors and photo of measuring pads with the guard-ring and DUT (V2).

Figure 3: Equivalent circuit for PN varactors (from anode, A, to cathode, C).

Figure 4: N-well BC resistances from the internal P^+ edges to the central N^+ diffusion. (a) R_{nw-1} . (b) R_{nw-2} .

Figure 5: Geometrical parameters for R_{nw-3} (2×2 BCs).

Figure 6: Modelled (with solid line for V1, dashed line for V2, and dotted line for V3) and numerically simulated (as the modelled adding squares, circles, and triangles for V1, V2, and V3, respectively) N-well resistance against the reverse bias voltage applied.

Figure 7: (a) Anode-to-cathode measured and modelled RF resistance against the operating frequency for V1 (with circles and solid line, respectively), V2 (with triangles and dashed line) and V3 (with squares and dotted line); $V_r = 1$ V. (b) Linear fitting of measured (with crosses) $|\omega \times \text{Im}(1/Y_{AC})|$ against ω^2 for V1 (with solid line), V2 (with dashed line), and V3 (with dotted line).

Figure 8: Modelled (as solid line, dashed line, and dotted line for V1, V2, and V3, respectively), and measured (as squares, circles, and triangles for V1, V2, and V3, respectively) quality factors against the applied reverse bias voltage. The corresponding modelled data excluding R_{nw} are represented by crosses; (a) $f = 5$ GHz and (b) $f = 10$ GHz.



TABLES

s	c	e	d_1	d_2
1.4	0.2	2.1	1.2	3.0

Table 1: BC geometrical parameters for R_{nw-i} ($i = 1, 2$; in μm)

Varactor(BCs)	a_1	a_2	b_1	b_2
V1(42)	24.0	15.0	51.9	34.6
V2(60)	17.1	29.4	38.9	62.8
V3(90)	33.6	22.0	71.4	48.7

Table 2: Geometrical parameters for R_{nw-3} (in μm)

Varactor(BCs)	V1(42)	V2(60)	V3(90)
R_{dc} (Ω)	2.3	2.1	1.4
α ($\times 10^{-21}$ Hz^{-2})	0.01	2.5	2.6
L (pH)	44	88	69

Table 3: Extrinsic parasitic components

ACCEPTED MANUSCRIPT
 ELSEVIER
 COPYRIGHT